Energy yield modelling of textured perovskite/silicon tandem photovoltaics with thick perovskite top cells

FABRIZIO GOTA,[1,2] **RAPHAEL SCHMAGER,**[1,2] **AHMED FARAG,**[1,2] **AND ULRICH W. PAETZOLD**[1,2,*]

[1]*Institute of Microstructure Technology, Karlsruhe Institute of Technology, Hermann-von-Helmholtz-Platz 1, 76344 Eggenstein-Leopoldshafen, Germany*
[2]*Light Technology Institute, Karlsruhe Institute of Technology, Engesserstrasse 13, 76131 Karlsruhe, Germany*
[*]ulrich.paetzold@kit.edu

Abstract: Recent advances in solution processing of micrometer-thick perovskite solar cells over textured silicon bottom solar cells allowed a new promising approach for the fabrication of 2T perovskite/silicon tandem photovoltaics, combining optimal light management in the textured bottom cell with the ease of solution processing. Detailed simulations are needed to assess the performances of this morphology configuration (thick perovskite configuration). In this work, in-depth optical and energy yield (EY) simulations are performed to compare the thick perovskite configuration with other relevant morphology configurations for 2T perovskite/silicon tandem photovoltaics. Under standard test conditions, the total photogenerated current of the thick perovskite configuration is 1.3 mA cm^{-2} lower (-3.4% relative) than the one of the conformal perovskite on textured silicon configuration for non-encapsulated cells and only 0.8 mA cm^{-2} (-2.1% relative) for encapsulated cells. Under realistic outdoor conditions, EY modelling for a wide range of locations shows that, while conformal perovskite on textured silicon configuration remains the optimal configuration, thick perovskite configuration exhibits a mere ~2.5% lower annual EY. Finally, intermediate scenarios are investigated with the angle of the perovskite front-side texture differing from the silicon texture and critical angles for efficient light management in these configurations are identified.

1. Introduction

In recent years, perovskite/silicon tandem solar cells have attracted wide attention from the photovoltaics research community and industry, having demonstrated higher record power conversion efficiencies (PCEs) (>29% reported [1,2]) than single junction (SJ) crystalline silicon (c-Si) solar cells [2,3]. The two sub-cells in perovskite/silicon tandem solar cells can be electrically connected in three different architectures, namely in a two-terminal (2T) [1,4–6], four-terminal (4T) [7–10], or three-terminal (3T) [11–14] architecture. In the 2T tandem architecture, the perovskite top cell is deposited directly on top of the c-Si bottom cell and is connected electrically in series via a recombination junction (RJ) [15] or a tunnel junction (TJ) [16]. This architecture has demonstrated so far the highest PCEs under standard test conditions (STCs) for perovskite/silicon tandem solar cells [17]. Moreover, this architecture has great potential for easy integration in c-Si solar module production, requiring only few additional steps for the deposition of the top cell layers over the bottom cell, while maintaining the same electrical contacting and wiring schemes compared to conventional silicon modules [18]. The main drawback of the 2T architecture is loss of current due to the presence of current-mismatch, which occurs when the currents of the top and

bottom cell at maximum power point (MPP) do not match [4]. Under realistic outdoor conditions, the spectral shape of the irradiance changes continuously and therefore current mismatch losses inevitably occur. Careful optimization of the perovskite thickness and bandgap is needed to minimize this effect [19].

To avoid current mismatch losses, the two sub-cells can be mechanically stacked and independently operated using the 4T architecture. However, the additional layers and the higher complexity in the balance of system (two inverters needed) lead to higher optical losses [14,20] and an increased cost of this technology. Recently, the 3T architecture has drawn increasing interest from the PV community. This architecture promises to solve, both, the issue of current mismatch losses for the 2T architecture and of optical losses and high fabrication complexity for the 4T architecture. Even if delivering the highest energy yield (EY) at the cell level [14], when connecting the cells together, end-string losses are expected [21] and therefore further research is required to assess the performances of the 3T architecture.

In view of the commercialization of perovskite/silicon tandem PV, which recent reports expect in the first half of the decade [22], the most advanced candidate architecture for the first generation of this technology is currently the 2T tandem architecture. The high reported efficiencies, along with the lower cost and lower complexity of fabrication and module interconnection, make 2T tandems the most promising first step for perovskite/silicon tandem solar cells [17] and, therefore, a very interesting candidate to investigate at this stage. In this study, we focus solely on 2T perovskite/silicon tandem solar cells. However, it is worth noting that the optical results presented here are also valid for monolithically integrated 3T tandem solar cells, since both architectures share the same morphology configurations for the silicon and perovskite sub-cells.

Even if extensively studied, the deposition of the perovskite top cell in 2T tandem solar cells has not been standardized yet. A variety of deposition techniques for the perovskite layer in a perovskite/silicon tandem solar cell are possible, including spin-coating [4,23], evaporation [24,25], blade coating [26], slot-die coating [27] and spray coating [28]. Moreover, the morphology and layer stack of the underlying bottom solar cells vary. For c-Si SJ solar cells, wafers undergo chemical etching after sawing to clean and texture (random pyramids with height > 5um) the front and rear surface, giving at the same time excellent optical properties to c-Si single junction modules [29]. However, direct deposition of conventional perovskite top cells (perovskite thickness ~500 nm) on textured c-Si modules presents different technological hurdles, that lead to increased probability of shunting and poor passivation of the interfaces of the top cell [30]. Therefore, the deposition of perovskite top cells for record perovskite/silicon tandem solar cells has been mostly performed on and optimized for silicon solar cells made from mechanically polished wafers [1,4,31]. Mechanical polishing the c-Si front surface has proved to facilitate overcoming the above-mentioned hurdles, delivering 2T perovskite/silicon tandem solar cells with extremely high fill factor (FF) values and low open-circuit voltage (V_{oc}) losses [1]. However, this approach is likely incompatible with large-scale fabrication, requiring expensive chemical mechanical polishing [32]. Moreover, the planar front surface causes higher optical losses than the textured one [19]. In 2018 Sahli et al. [33] demonstrated for the first time a fully textured perovskite/silicon tandem solar cell, using a hybrid two-step process that combined co-evaporation of a porous lead iodide (PbI_2) and ceasium bromide (CsBr) template and spin-coating an organohalide solution composed of formamidinium iodide (FAI) and formamidinium bromide (FABr). The tandem cell delivered a record short-circuit current density (J_{sc}) of 19.5 mA cm^{-2}. Even if very promising and innovative, this approach has not yet proved capable of matching the electrical performances, i.e. low V_{oc} losses and high FF, of the planar front-side tandem configuration. Moreover, the two-step process involved at this stage spin-coating, which is incompatible with large area deposition. Better suited for up-scaling is evaporation processing. Although promising results in this direction have been demonstrated, 2T tandem solar cells with conformally deposited perovskite top cells over fully textured silicon

bottom cells do not still match the electrical performances of record 2T tandem solar cells with planar c-Si front-side.

Recently, a new approach, consisting in depositing a solution-processed thick perovskite layer on a fully textured silicon bottom cell, covering completely the pyramids, has been demonstrated [26,27,34–37] and quickly gained attention. With this approach, the perovskite layer does not follow conformally the morphology of the underlying pyramidal textures. Indeed, the front-side of the perovskite layer is planar or follows the underlying textures with a moderate angle. Spin-coating, blade coating and slot-die coating have proven to enable the fabrication of high-efficiency cells using this new approach and a record 2T tandem solar cell with a PCE equal to 28.6% has been recently achieved [37] (see Table 1 for a direct comparison of record perovskite/silicon tandem solar cells with different morphologies). To allow the deposition of the perovskite layer on a fully textured substrate, the size of the pyramidal textures needs to be reduced in the range of 1–2 µm or below. Moreover, the charge-carrier diffusion length in the thick perovskite layer needs to be increased to allow efficient charge carrier extraction for micrometer-thick absorber layers. Only in recent years this has been achieved. Eggers et al. [38] reported high-efficiency inkjet-printed perovskite solar cells with large columnar grains and thicknesses > 1µm in 2019. In 2020, Chen et al. used additives to increase the electron-diffusion length to 2.3 µm [39], while Hou et al. passivated the perovskite surface via exposure to 1-butanethiol vapor [34]. This approach allows the deposition of solution-processed perovskite layer with large-scale deposition techniques on a fully textured c-Si substrate, combining the excellent optical properties and low fabrication cost of fully textured c-Si bottom cells and allowing fast and reliable large-scale deposition techniques for the perovskite top cell. Moreover, solution-processing, compared to evaporation processing, offers a flexible and wide range of different precursors' compositions for band gap tuning, additives implementation for bulk and surface passivation, in addition to lower energy consumption [40].

Table 1. STCs performances of record perovskite/silicon tandem solar cells with different morphology configurations. For consistency, the perovskite bandgap is always computed from the inflection point of the top cell EQE curve, as suggested by Krückemeier et al. [43]. For J_{sc}, V_{oc} and FF, the average value obtained from forward and reverse I-V scan is used. Finally, the cell efficiency η is taken from steady-state maximum power point (MPP) measurements.

	Morphology configura-tion	Perovskite Thickness [nm]	Perovskite Bandgap [eV]	J_{sc} [mA cm^{-2}]	V_{oc} [V]	FF [%]	η_{MPP} [%]
Al-Ashouri et al., 2020 [1]	Planar	500[b]	1.68	19.2	1.90	79.1	29.2
Aydin et al., 2020 [5]	Conformal	400[b]	1.65	19.8	1.73	72.5	25.0
Aydin et al., 2021 [36]	Thick	1000[b]	1.67	19.5	18.3	74.2	26.8
Chen et al., 2020 [26][a]	Thick	1200[b]	1.67	19.2	1.82	74.9	26.1
De Bastiani et al., 2020 [35]	Thick	1000[b]	1.68	18.5	1.80	75.7	25.2
Hou et al., 2020 [34]	Thick	1100[c]	1.67	19.1	1.79	74.5	25.7
Köhnen et al., 2019 [4]	Planar	500[b]	1.64	19.2	1.77	76.6	26.0
Liu et al., 2021 [37]	Thick	900[c]	1.68	19.6	1.86	78.4	28.6
Mazzarella et al., 2019 [31]	Planar	600[c]	1.65	19.0	1.79	74.5	25.4
Nogay et al., 2019 [44]	Conformal	450[b]	1.65	19.5	1.74	74.1	25.1
Sahli et al., 2018 [33]	Conformal	440[c]	1.64	19.5	1.79	71.1	25.2

[a]With textured PDMS on front-side
[b]Estimated from SEM images
[c]Reported in manuscript

In order to study optical properties and performances under realistic conditions for different morphology configurations, a detailed simulation study is required. In response to this need,

we use our in-house developed open source EY modelling platform named EYcalc [41,42]. EY modelling is essential to assess the performance of tandem solar cells under realistic conditions. Long-term outdoor measurements of perovskite/silicon tandem solar cells are hindered by stability issues of the perovskite top cell. Moreover, making a fair comparison of the performances and optimizing perovskite layer properties, as thickness and bandgap, for different morphology configurations would require a huge experimental effort. In laboratory conditions such studies are easier to carry out, being performed under STCs. However, real outdoor conditions, where the intensity, angle of incidence and spectral shape of the incoming irradiation is continuously changing, vary significantly from STCs. This leads to large differences in optimum perovskite thickness and bandgap between STCs and outdoor irradiation conditions [19].

In this study, we investigate the optical and EY performances of 2T perovskite/silicon tandem solar cells with thick perovskite layer (henceforth referred to as 'thick perovskite configuration', see schematics in Fig. 1(b)) using the above-mentioned EY modelling platform. We compare these performances with those of 2T perovskite/silicon tandem solar cells with planar c-Si front-side ('planar configuration', Fig. 1(a)) and with conformal perovskite on textured c-Si ('conformal perovskite configuration', Fig. 1(c)). We study both non-encapsulated tandem solar cells and encapsulated tandem solar cells. We then define the optimum band gap and the required perovskite film thickness that result in the highest EY for each morphology under different irradiation conditions. Finally, we analyze the case of 2T tandem solar cells on fully textured c-Si substrates with perovskite layers with intermediate front-side angle, i.e. neither fully conformal nor fully planar perovskite front-side interface. The dominant optical phenomena for non-encapsulated and encapsulated are shown and design rules are suggested.
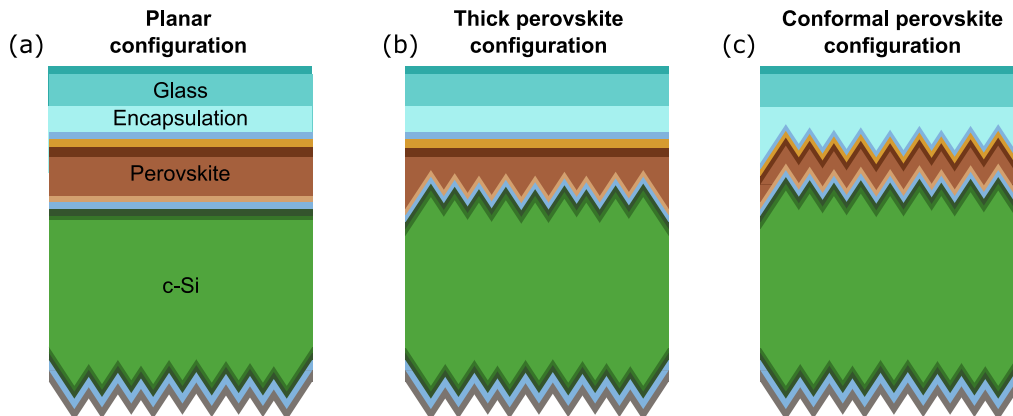
Fig. 1. Schematic cross-section of encapsulated 2 T perovskite/silicon tandem solar cells with planar (a), thick perovskite (b) and conformal perovskite (c) morphology configurations.

2. Methods

The EYcalc energy yield modelling platform used for this work comprises four different modules: (i) irradiance module, (ii) optics module, (iii) electrics module and (iv) energy yield core module. The irradiance module calculates the spectrally and angularly resolved direct and diffuse irradiance spectra for a typical meteorological year for hundreds of locations in the USA. To this end, we use hourly-resolved typical meteorological data (TMY3) [45] from National Renewable Energy Laboratory (NREL). We then combine the simple model of atmospheric radiative transfer of sunshine (SMARTS) [46] with a cloud model to obtain the desired hourly-resolved irradiance from the TMY3 data. Subsequently, the optics module computes spectrally and angularly resolved absorptance, reflectance and transmittance for the layer stack under study using a combination

of the transfer-matrix method for thin film layers and a series expansion of the Beer-Lambert law for optically incoherent layers. To take into account textured interfaces, we use geometrical ray-tracing, following the approach of Baker-Finch & McIntosh [47]. The optical response of the textures is simulated in the ray optics limit and therefore is valid for textures with dimensions larger than the wavelength of light in the material of propagation ($\lambda = \lambda_0/n$, with λ_0 being the wavelength of light in vacuum and n the real part of the refractive index of the material). For much smaller textures one would need to consider the evanescent fields and treat the optical response of the texture in a rigorous electromagnetic simulation. Then the energy yield module, using the irradiance and optics data from the above-discussed modules, computes the photogenerated current density (J_G) for the two sub-cells for each hour of the typical meteorological year, taking into account the solar cell rotation and tilt. Next, the electrics module determines the hourly-resolved temperature-dependent current density-voltage (*J-V*) characteristics and the maximum power point (MPP). For this module, it is possible to use either an analytical one-diode model or a more accurate numerical approach. In this paper we use the latter approach, via LTspice [48], to perform the electrical simulations. To estimate the cell temperature, we use the Nominal Operating Cell Temperature (NOCT) model [49]. For this model, we assume a NOCT of 48°C, while the insolation on the cell and the ambient air temperature are extracted from TMY3 data. Temperature effects on *J-V* curve are taken into account by using temperature dependent diodes in LTspice electrical simulations. Temperature-induced EQE variations due to bandgap shift are instead not taken into account. Finally, the energy yield module delivers the final annual EY result taking into account the contributions of all the hours of the typical meteorological year.

To validate the results of our optics module for the different morphology configurations, in Fig. S1 of Supplement 1 we show the comparison between the EQE of three experimental cells with different morphology configurations and the absorptance obtained from our simulations. If we compute the total photogenerated current $J_{G,total}$ by integrating the EQE over an AM1.5G spectrum, we find that the differences in $J_{G,total}$ between simulated and experimental cell is <0.7% for each of the three configurations. Since these values are smaller than the PCE and EY relative differences presented in this work, we conclude that our model is appropriate for a comparison between the three configurations.

An overview of the parameters used in the electrical simulations is shown in Fig. S2 of Supplement 1.

A more detailed description of the energy yield platform can be found in a previous publication [42], while the EYcalc software is available as source code online [41].

3. Results and discussion

To assess the optical and EY performances of 2T perovskite/silicon tandem solar cells with thick perovskite, conformal perovskite and planar morphology configurations, we modelled the cells in our EYcalc simulation platform using the same layer stack (see Fig. 2(a)). The only difference between the three configurations is the morphology of the c-Si front-side and the morphology of the perovskite layer. All the remaining thin films in between the two sub-cells and on top of the perovskite layer are considered as perfectly conformal to the underlying layers. In the following, both encapsulated cells and non-encapsulated cells will be addressed to investigate the differences between laboratory-scale cells, generally without encapsulation, and encapsulated cells, which are used in outdoor applications. In non-encapsulated cells, the ethylene-vinyl acetate (EVA) and glass layers are removed and the 100 nm MgF_2 layer, which serves as an anti-reflection coating, is conformally deposited on the 120 nm IZO layer (see Fig. S3 of Supplement 1 for a schematic cross-section of the layer stack for non-encapsulated cells). The layer stack used for the three morphology configurations follows largely the one presented by De Bastiani et al. [35]

in their work on bifacial perovskite/silicon tandem solar cells with thick perovskite top solar cells processed on fully textured c-Si bottom cell.
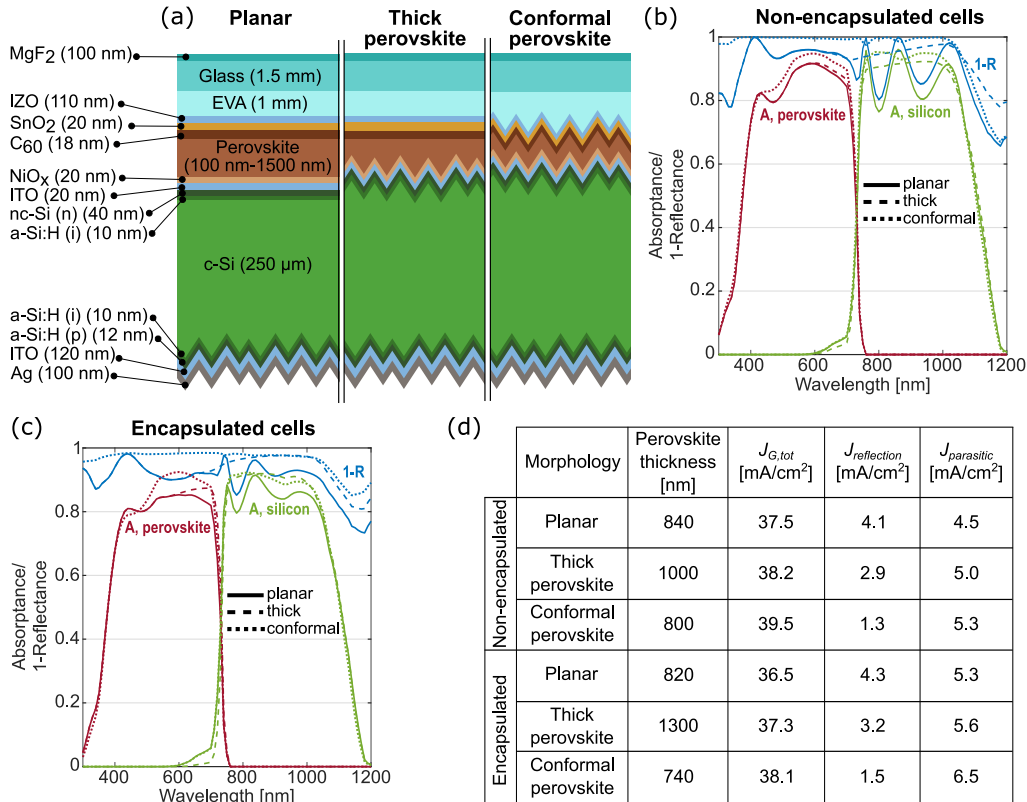
Fig. 2. (a) Schematic cross-section showing the layer stacks used in this study for encapsulated perovskite/silicon tandem solar cells with planar, thick perovskite and conformal perovskite morphologies. Absorptance and reflectance curves for the three perovskite morphologies without (b) and with (c) encapsulation. The perovskite bandgap is set to 1.70 eV and the perovskite thickness is optimized for current matching. The main results of the optical simulations are presented in (d).

3.1. Comparison of optical performances

The optical performances of the three morphology configurations vary significantly between non-encapsulated and encapsulated cells. For non-encapsulated cells, incoming photons impinge directly on the textured interface for the conformal perovskite configuration, thereby reducing reflection losses. Indeed, the textured front-side of the non-encapsulated cells forces the incoming photons to impinge several times by multiple reflections on the air/MgF$_2$/IZO interface, leading to excellent light in-coupling [50]. Therefore, the conformal perovskite configuration exhibits the lowest reflection losses $J_{reflection}$ and the highest total photogenerated current density $J_{G,total}$ in the two absorber layers. For a perovskite bandgap of 1.70 eV, $J_{reflection} = 1.3$ mA cm^{-2} and $J_{G,total} = 39.5$ mA cm^{-2}, respectively. For planar and thick perovskite configurations, reflection losses and absorptance for the top cell (300 nm – 700 nm) are comparable, with the exception of the larger and steeper absorptance in the wavelength range close to the bandgap of the thick perovskite configuration due to the larger optimum perovskite thickness. However, for the bottom cell, the fully textured c-Si in the thick perovskite configuration enables excellent

light in-coupling and light trapping, while for the planar configuration, interference fringes, caused by the planar c-Si front-side, are clearly visible. As a consequence, the thick perovskite configuration shows lower $J_{reflection}$ (2.9 mA cm^{-2}) and higher $J_{G,total}$ (38.2 mA cm^{-2}) than the planar configuration ($J_{reflection}$ = 4.1 mA cm^{-2}, $J_{G,total}$ = 37.5 mA cm^{-2}). It has been demonstrated that a nanocrystalline silicon oxide (nc-SiO$_x$) layer can dampen infrared interferences and reduce reflection losses for the planar configuration [31,51]. In this work, however, we decide not to perform an optical optimization and use the same layer stack for all three configurations for the sake of fair comparison.

Contrary to the previous scenario, for encapsulated cells, which are more relevant considering real world applications, the front-interface is always constituted by a planar MgF$_2$/glass/EVA stack. Moreover, the front glass and EVA layer introduce additional parasitic losses of ∼1 mA cm^{-2}. Therefore $J_{G,total}$ is lower for all the configurations. It should be noted that alternative ARC than MgF$_2$ are mostly used in commercial modules, but this does not affect the study and conclusions presented here. The largest loss compared to the non-encapsulation scenario is associated with the conformal perovskite configuration, since with the encapsulation, reflection losses in the 300 nm – 1000 nm range are greatly increased (see Fig. 2(c)). Nevertheless, this configuration still achieves the highest $J_{G,total}$ (38.1 mA cm^{-2}) due to the excellent light management properties derived from the fully textured c-Si and perovskite layers. The lower losses in $J_{G,total}$ compared to the non-encapsulated scenario allow the remaining two configurations to partially close the gap with the conformal perovskite configuration. Indeed, $J_{G,total}$ = 37.3 mA cm^{-2} for the thick perovskite configuration (only 0.8 mA cm^{-2} lower than the conformal perovskite configuration), while $J_{G,total}$ = 36.5 mA cm^{-2} for the planar configuration.

It is worth noting that, for both non-encapsulated and encapsulated cells, the optimum perovskite layer thickness that results in current matching is considerably higher in the thick perovskite configuration than in the planar and conformal perovskite configurations (see Fig. 2(d)). Due to the combination of high absorptance in the bottom cell (good light in-coupling in the bottom cell due to textured c-Si front-side) and relatively low absorptance in the top cell (mostly due to reflection losses caused by the planar perovskite front-side), the ratio between the photogenerated current in the top and bottom cell ($J_{G,perovskite}/J_{G,silicon}$) is the lowest among the three configurations. Therefore, to compensate for this effect, a thicker perovskite layer is required or, alternatively, a narrower perovskite bandgap.

To further increase the current generation in the cells, a textured glass or a textured poly-dimethylsiloxane (PDMS) layer can be used on the front side of the cell. Chen et al. [26] demonstrated that a textured front PDMS layer on top of a perovskite/silicon tandem solar cell with thick perovskite configuration can significantly increase $J_{G,total}$. The focus of this work is modelling solar cells in realistic outdoor conditions based on existing and widely used module technologies. Therefore, only the three configurations shown in Fig. 2(a) are investigated in great detail. However, optical results for cells with thick perovskite configuration and textured front PDMS are discussed in Supplement 1 (see Fig. S4 and Table S1) to give a brief overview of the optical advantages of this configuration.

3.2. Perovskite bandgap and thickness optimization

Having studied the optical properties of the three configurations for a specific perovskite bandgap, we optimize each configuration by changing both the perovskite bandgap and thickness. Moreover, we investigate the different trends for non-encapsulated and encapsulated cells and under STCs and realistic outdoor conditions. For these simulations, we sweep the perovskite bandgap from 1.59 eV to 1.89 eV, while the perovskite thickness from 100 nm to 1500 nm. It should be noted that there are practical limitations to the thickness of the perovskite layer. For the conformal perovskite configuration, achieving high-quality thick perovskite layers with efficient charge carrier extraction can be very challenging, due to constraints of evaporation processing, which,

among others, hinders the use of additives. Up to now, the reported experimentally fabricated cells are limited to perovskite thicknesses of ~500 nm [5,33,44]. We choose here thicknesses up to 800 nm. On the contrary, for the thick perovskite configuration, there are limitations for the minimum perovskite thickness, which should be large enough to fully cover the underlying pyramidal textures. Alasfour et al. [52] have demonstrated the realization of sub-μm pyramidal textures realized with conventional alkaline-based wet-chemical etching processes. By tuning the etching processes, the fabrication of pyramidal textures with average height between 62 nm and 512 nm was accomplished. However, only wafers with pyramidal textures having average height larger than ~400 nm showed light trapping and surface defect densities comparable to standard textured c-Si wafers. In this work, we set the minimum perovskite thickness for thick perovskite configuration to 800 nm. Finally, for all configurations, a maximum thickness for the perovskite layer had to be fixed due to lower charge carrier extraction efficiency with increasing perovskite thicknesses. In this study, we set the maximum perovskite thickness to 1.5 μm.

We first start by optimizing the PCE in STCs for non-encapsulated cells. The highest PCE is achieved by the conformal perovskite configuration (26.9%), followed by the thick perovskite configuration (26.3%) and the planar configuration (25.8%). The highest limit for the perovskite thickness in the latter two configurations allows to narrow the performance gap with the conformal perovskite configuration, which exhibits 2.3% relative higher PCE compared to 3.4% relative higher $J_{G,total}$ than the thick perovskite configuration and 4.3% relative higher PCE compared to 5.3% relative higher $J_{G,total}$ than the planar configuration. A thicker perovskite implies a larger share of photons absorbed in the top cell. Consequently, current matching is achieved using a wider perovskite bandgap, with a positive effect on the PCE. It is worth reminding that wide-bandgap perovskite compositions suffer from degradation problems [53]. In this regard, the thick perovskite configuration offers an advantage over the other two configurations, when using the same thickness, due to the lower $J_{G,perovskite}/J_{G,silicon}$ ratio, as explained in the previous paragraph. To optimize the PCE for the thick perovskite configuration, it is required a perovskite layer with, on average, a ~10 meV narrower bandgap than the conformal perovskite configuration and ~18 meV narrower than the planar configuration (see Fig. S5 of Supplement 1). This allows the thick perovskite configuration to have an optimum perovskite bandgap (1.73 eV) comparable to the optimum for the conformal perovskite configuration (1.72 eV), even if the latter has a significantly thinner perovskite layer. Finally, the planar configuration shows the highest optimum perovskite bandgap, at 1.75 eV.

For encapsulated cells, the optimum bandgap shifts to lower values. Since the EVA and glass layers introduce parasitic absorption losses mainly in the short wavelength range, a thicker perovskite layer, or alternatively a narrower perovskite bandgap, compared to the non-encapsulated scenario is required to achieve current matching. The highest PCE is achieved by the conformal perovskite configuration (26.0%, optimum bandgap $E_G = 1.72$ eV), followed by the thick perovskite configuration (25.5%, optimum $E_G = 1.72$ eV) and the planar configuration (25.1%, optimum $E_G = 1.73$ eV). Here, the relative PCE gain of the conformal perovskite configuration with respect to the thick perovskite configuration is 2.0%, while it is 3.6% with respect to the planar configuration.

Next, we investigate the performance of the cells under realistic irradiation conditions. We perform EY simulations for the encapsulated cells at the exemplary location of Phoenix, Arizona. For all the configurations, we observe a shift of the optimum perovskite thickness to lower values and a shift of the optimum perovskite bandgap to higher values compared to the STC scenario, when keeping respectively the same perovskite bandgap and thickness. This is due to the irradiation spectra under realistic outdoor conditions, which cause a larger share of light across the year to be collected by the top cell. While for STCs only direct irradiation is relevant, under realistic conditions also diffuse irradiation is considered. The latter has a higher share of high energy photons, due to Rayleigh scattering taking place in the atmosphere (see Fig. S6 of

Supplement 1 for a detailed explanation of how direct and diffuse irradiance has been calculated). To balance this blue-shift of the spectra in the performance of 2T perovskite/silicon tandem solar cells, a lower perovskite thickness or, alternatively, a wider perovskite bandgap is needed.

The highest annual EY is achieved by the conformal perovskite configuration (504 kWh m^{-2}, optimum E_G = 1.76 eV), followed by the thick perovskite configuration (491 kWh m^{-2}, optimum E_G = 1.76 eV) and the planar configuration (480 kWh m^{-2}, optimum E_G = 1.77 eV). The relative performance difference, in percentage, between the three configurations is slightly higher under realistic conditions compared to STCs, due to the better light management of the conformal perovskite configuration at large angles of incidence. Indeed, the EY for the conformal perovskite configuration is 2.6% higher compared to the thick perovskite configuration and 5.0% higher compared to the planar configuration (2.0% and 3.6% relatively higher PCE under STCs). Even under realistic irradiation conditions, we observe a lower optimum perovskite bandgap for the thick perovskite configuration, when considering the same perovskite thickness for the three morphology configurations. On average, the optimum perovskite bandgap for the thick perovskite configuration is ~15 meV narrower than the planar configuration and ~20 meV narrower than the conformal perovskite configuration (see Fig. S5 of Supplement 1).

In the previous simulations, we did not take into account in the optical simulations the temperature dependence of the bandgap for the two sub-cells. Aydin et al. [5] reported that with increasing temperatures, the silicon bandgap narrows, while the perovskite bandgap widens. This effect shifts the optimum perovskite bandgap, measured at room temperature, to lower values. However, there are still insufficient data for different perovskite compositions or bandgaps and a solid knowledge and description of these effects is still lacking. The effects of temperature only shift the optimum perovskite bandgap and thickness in the same direction for all configurations. In Fig. S7 of Supplement 1, we modelled these effects by using temperature coefficients for the short-circuit current densities of the two cells based on the experimental results presented in the work of Aydin et al. [5]. We observed in that case a shift of the optimum perovskite bandgap to lower values of ~15 meV, when using the same thickness. The general trends, presented in Fig. 3, remain nevertheless valid.

3.3. Energy yield under different climatic conditions

To validate the generality of the results presented above, we perform EY simulations in several locations under different climatic conditions. For each location and configuration, we optimize the perovskite bandgap and thickness. For all the locations, the conformal perovskite configuration achieves the highest EY (see Fig. 4(a)). The relative gain with respect to the thick perovskite configuration ranges from 2.2% to 2.8%, while it is from 4.5% to 5.3% with respect to the planar configuration. If we assume for the conformal perovskite configuration a perovskite thickness limit of 1500 nm, these relative gains increase to 2.8% - 3.8% with respect to the thick perovskite configuration and 5.1% - 6.3% with respect to the planar configuration. Overall, these simulations indicate that the difference in performance between the three configurations do not show a large dependence on climatic conditions.

However, the optimum perovskite bandgap and thickness do show a dependence on location (see Fig. 4(b)), due to variations of the irradiance spectra. Previous studies have already confirmed that in perovskite-based tandem solar cells, the optimum perovskite bandgap and thickness is correlated with the average photon energy (APE) of the irradiation spectrum [54]. Among the locations investigated in Fig. 4(a), the difference in optimum bandgap is as large as 40 meV between Phoenix and Anchorage. Still, the location dependence of optimum perovskite thickness and bandgap does not have a large impact on EY. If an average perovskite bandgap (here 1.75 eV is chosen) and thickness (800 nm for the conformal perovskite configuration, 1500 nm for the remaining two configurations) are selected, the EY loss of each configuration with respect to the optimized cell is <1% for all locations, with the exception of Anchorage. In the latter location,
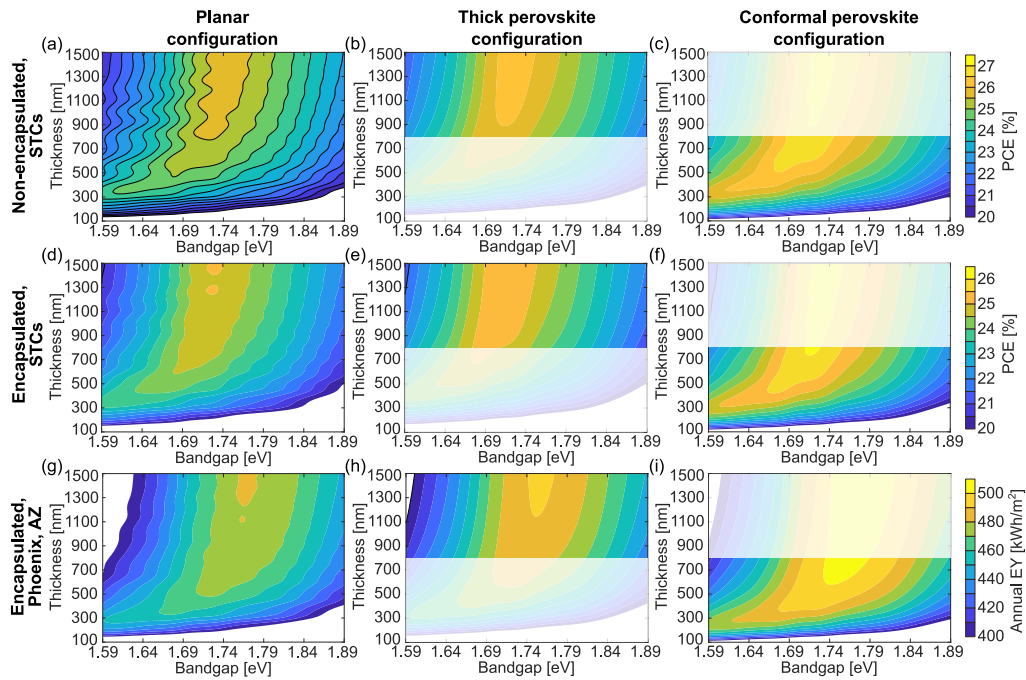
Fig. 3. Contour plots showing the PCE as a function of perovskite bandgap and thickness for non-encapsulated tandem solar cells with planar (a), thick perovskite (b) and conformal perovskite (c) morphologies. Analogous contour plots for encapsulated tandem solar cells with planar (d), thick perovskite (e) and conformal perovskite (f) morphologies. Contour plot showing the annual EY in Phoenix, Arizona as a function of perovskite bandgap and thickness for encapsulated tandem solar cells with planar (g), thick perovskite (h) and conformal perovskite (i) morphologies. For the thick perovskite and conformal perovskite configurations, we shaded the thickness regions outside the limit that we assumed in this paper (minimum perovskite thickness of 800 nm for the first one, maximum 800 nm for the second one).
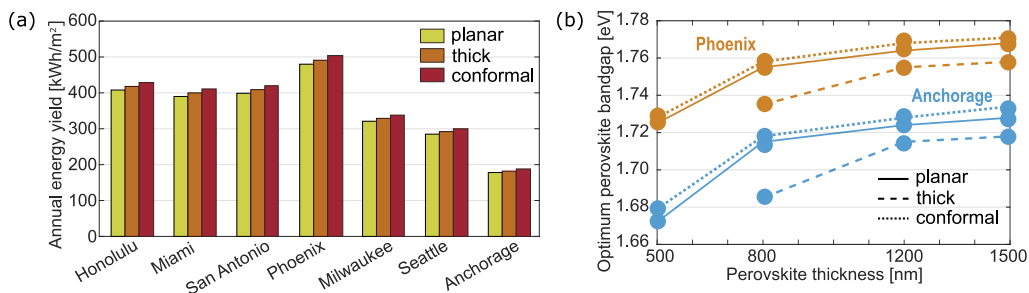
Fig. 4. (a) Annual EY for the three tandem morphology configurations for several cities in the USA under different climatic conditions. (b) Optimum bandgap for the three tandem morphology configurations in Phoenix and Anchorage for different perovskite thicknesses.

the exceptional irradiation conditions impose a narrower bandgap, resulting in EY losses of 2–3%. The difference in the optimum bandgap for different morphology configurations, instead, is not location dependent. For all locations, the thick perovskite configuration requires the lowest bandgap for a fixed perovskite thickness, while the conformal perovskite configuration requires the highest bandgap.

3.4. Intermediate perovskite front-side angles

Up to now, we assumed for the thick perovskite configuration a planar perovskite front-side and for the conformal perovskite configuration a perfectly conformal perovskite layer. In practice, for experimental cells, the perovskite layer can follow the profile of the underlying textures with intermediate angles [35], depending on the deposition technique and its experimental parameters. It is therefore interesting to study the optical and EY performance of tandem solar cells as a function of the angle θ_p of the textures of the perovskite layer front-side (see Fig. 5(a) and 5(d) for a graphical representation of θ_p).

Encapsulated and non-encapsulated cells are very differently affected by the change of θ_p. In non-encapsulated cells, photons impinge directly on the thin film layers on top of the perovskite layer. When this interface is textured, multiple bounces at the front interface can take place, increasing light in-coupling. While morphologies with $\theta_p < 30°$ achieve $J_{G,total} \approx 38.4$ mA cm^{-2}, starting from $\theta_p \approx 45°$, $J_{G,total} \approx 39.5$ mA cm^{-2} (see Fig. 5(c)). For comparison, the total photogenerated current in the planar morphology is equal to 37.5 mA cm^{-2}. To comprehend the nature of this trend, we use ray tracing simulations (via OPAL 2, see Fig. S8 of Supplement 1). For $\theta_p \leq 30$, only a single bounce occurs on the front interface, leading to inefficient light in-coupling. Consequently, the reflectance is relatively high. For larger angles, an increasing share of the photons experiences a double bounce, as in case (i) in Fig. 5(a). Starting from $\theta_p = 45°$, all photons bounce at least twice on the front-side interface, as in case (ii) in Fig. 5(a). This transition is clearly visible in the absorptance of the perovskite and silicon layers (see Fig. 5(b)) and therefore also in the total photogenerated current $J_{G,total}$ of the tandem cell. From these results we deduce that achieving a high degree of conformality, close to the ideal case for c-Si textures ($\theta_p = 54.74°$), is highly beneficial for the optical performance of non-encapsulated tandem cells.

In the scenario of encapsulated cells, photons always imping on a planar air/MgF$_2$/glass interface. Here, the dominant optical effect for the absorptance (see Fig. 5(e)) and $J_{G,total}$ (see Fig. 5(f)) is the minimization of light out-coupling (see Fig. 5(d)) after having been reflected back at the textured perovskite front-side interface (at the corresponding IZO/SnO$_x$/C$_{60}$/perovskite stack). We can observe from Fig. 5(f) that there is a sharp increase in the total photogenerated current $J_{G,total}$ starting from $\theta_p \approx 21°$. This is explained by total internal reflection.

When photons impinge on a glass/air interface with an angle larger than ~42°, they experience total internal reflection. With the inclusion of the MgF$_2$ layer, the reflectance for angles larger than ~42° in the 300 nm – 1200 nm range is not complete, but still considerably high (> 96%), while for slightly lower angles, the average reflectance is much lower. For example, for an angle of 40°, the average reflectance is ~25% (see Fig. S9 of Supplement 1 for the reflectance for different angles of incidence at glass/air and glass/MgF$_2$/air interface). Since normally incident light impinging on perovskite front-side textures with angle θ_p will then be reflected back with an angle $2\theta_p$ towards the glass/MgF$_2$/air interface, we observe a sharp increase in $J_{G,total}$ for $\theta_p >$ ~21°. Therefore, for encapsulated cells, a relatively poor conformality of the perovskite layer is sufficient to maximize the total photogenerated current in STCs.

It is important to note that the analysis we made in the previous paragraphs is valid only for light at normal incidence (i.e. with angle of incidence (AOI) 0°). Under realistic outdoor conditions, the direct light from the sun comes with an angle and the diffuse light impinges on the panel from a wide range of AOI. For large AOI, a high degree of conformality is desirable to
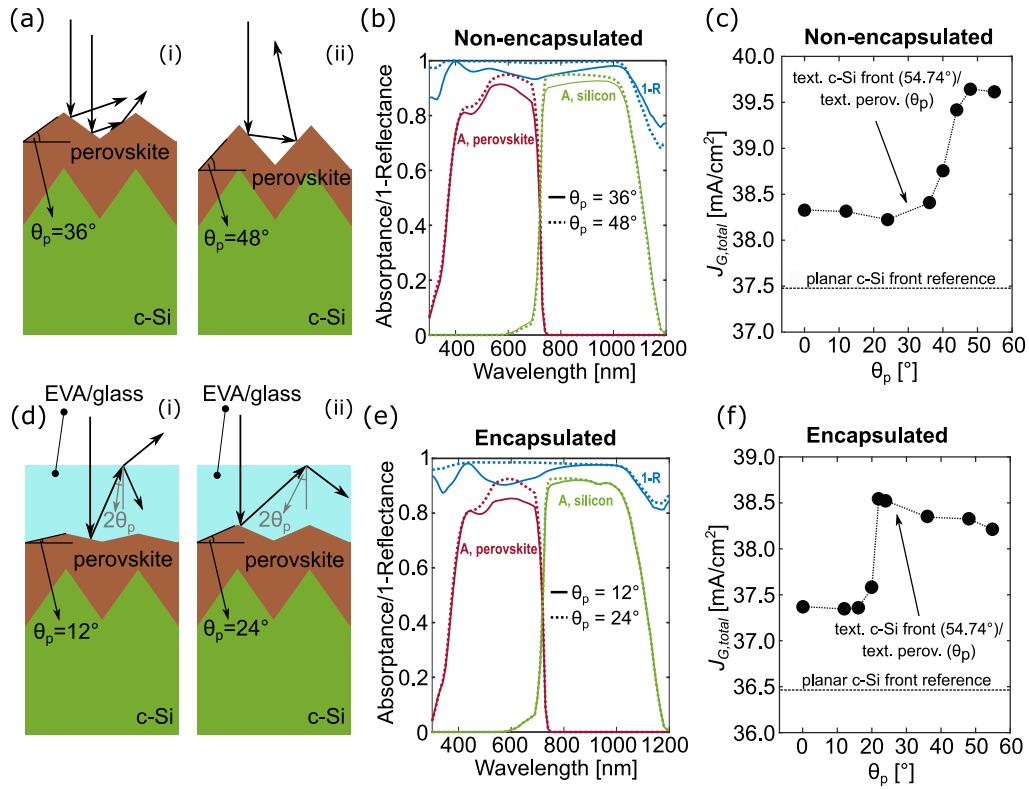
Fig. 5. (a) Schematic illustration of light reflection at the front interface for non-encapsulated tandem solar cells and normal light incidence. For perovskite front-side angles $\theta_p < 45°$ (i), all photons or a part of the incoming photons bounce only once at the perovskite front-side interface. For $\theta_p > 45°$ (ii), all incoming photons reflected at the perovskite front-side interface impinge again on another pyramid, thus substantially increasing light in-coupling. (d) Schematic illustration of light out-coupling for encapsulated tandem solar cells and normal light incidence. When photons are reflected back at the perovskite front-side interface, if $\theta_p < \sim 21°$ (i), part of these photons will exit the solar cell. When $\theta_p > \sim 21°$ (ii), all the photons experience total internal reflection, thus drastically reducing reflection losses. In (a) and (d) the thin film layers on top of the perovskite layer and between the perovskite and c-Si are not shown for simplicity. Absorptance and reflectance for non-encapsulated (b) and encapsulated (e) tandem solar cells for different perovskite front-side textures angles θ_p. Total photogenerated current in the perovskite and silicon absorber layers $J_{G,total}$ for different morphologies for non-encapsulated (c) and encapsulated (f) tandem solar cells. For all the simulations in this figure, the perovskite bandgap is set to 1.73 eV and the perovskite thickness is 800 nm.

maximize the total photogenerated current (see Fig. 6(a) and 6(b) and Fig. S10 of Supplement 1). To investigate the effects of realistic irradiation conditions, we perform EY simulations for different intermediate angles and morphology configurations in Phoenix, Arizona. We set the perovskite bandgap to 1.73 eV and we optimize the perovskite thickness for each morphology configuration. In this scenario, the transition to higher EY for larger θ_p is more gradual (see Fig. 6(c)). The highest EY value is found for the conformal perovskite configuration. This is due to the efficient light management for large AOI. However, also under realistic conditions it is demonstrated that perfect perovskite conformality is not necessary to achieve high EY values. Already with $\theta_p = 24°$, the annual EY is 99.2% of the EY for the conformal perovskite configuration.
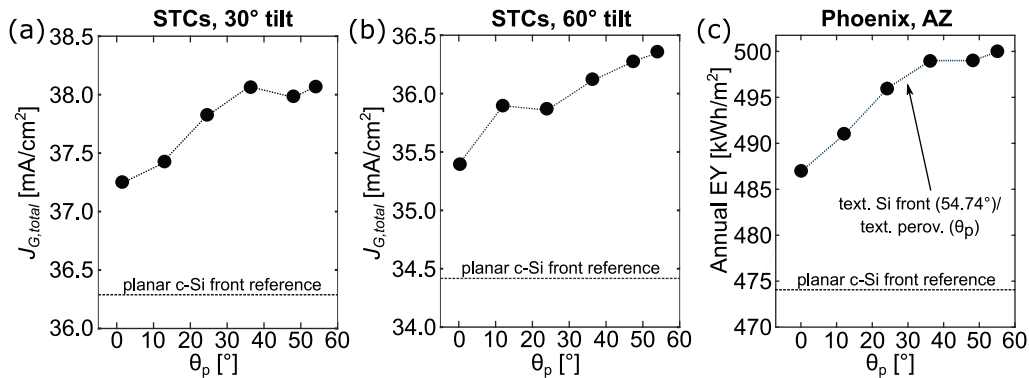
Fig. 6. Total photogenerated current in the perovskite and silicon absorber layers $J_{G,total}$ for different morphologies for encapsulated tandem solar cells under AM1.5G spectrum with a solar cell tilt angle of 30° (a) and 60° (b). (c) Annual EY in Phoenix, Arizona for different morphology configurations for encapsulated tandem solar cells as a function of θ_p. For all the simulations in this figure, the perovskite bandgap is set to 1.73 eV. The perovskite thickness is set to 800 nm in (a),(b), while it is optimized for each θ_p point in (c).

Overall, the thick perovskite configuration opens a new route for solution processing of perovskite absorber layers for perovskite/silicon tandem solar cells. While the conformal perovskite configuration still offers the highest optical and EY performances, the thick perovskite configuration exhibits only ~2.5% lower EY under different climatic conditions with an encapsulated stack. If the perovskite layer is deposited in such a way that it follows the underlying silicon pyramidal textures (with characteristic 54.74° angle) with a lower angle θ_p, the difference in EY performance with the conformal perovskite configuration substantially decrease even with relatively low values of θ_p. Already with $\theta_p = 24°$, the EY is <1% lower than calculated for the conformal perovskite configuration. Moreover, the thick perovskite configuration shows better optical and EY performances compared to the planar configuration. These results, and the use of industrially relevant fully textured silicon wafers, make the thick perovskite configuration attractive for industrial fabrication of perovskite/silicon tandem solar cells. Therefore, the continued development of the thick perovskite configuration is encouraged. New solutions to increase the V_{oc} and FF of experimental cells, by optimizing the window layers and maximizing the charge collection efficiency, are required to match the performances of planar configuration cells. Finally, investigating and optimizing deposition techniques that produce thick perovskite layers with non-planar front-surfaces would lead to an increase of the EY in outdoor applications, closing the performance gap with the conformal perovskite configuration.

4.　Conclusion

This study presents optical and energy yield (EY) simulations for 2T perovskite/silicon tandem solar cells with thick perovskite layers on fully textured c-Si bottom cells (thick perovskite configuration). A comparison with the performances of 2T perovskite/silicon tandem solar cells with alternative morphologies, namely planar configuration and conformal perovskite configuration, is presented.

The performances of the thick perovskite configuration are comparable to the performances of the conformal perovskite configuration, with the latter achieving the best optical and EY results. In particular, for non-encapsulated cells, the textured front interface of the conformal perovskite configuration decreases reflection losses. As a result, under AM1.5G spectrum, the total photogenerated current density $J_{G,total}$ for the thick perovskite configuration is equal to 38.2 mA cm^{-2}, while for the conformal perovskite configuration reaches 39.5 mA cm^{-2} (+3.4%). Encapsulated cells present a planar MgF$_2$/glass/EVA front interface, therefore limiting the advantages of the conformal perovskite configuration. The performance gap between the two configurations here is narrower, with a difference in $J_{G,total}$ of only 0.8 mA cm^{-2} (+2.1%). Finally, under realistic irradiation conditions, the annual EY gain of the conformal perovskite configuration over the thick perovskite configuration ranges from 2.2% to 2.8% for different climatic conditions.

The performances of the thick perovskite configuration can be further enhanced by changing the angle θ_p of the textures at the perovskite front-side interface. For non-encapsulated cells, a 1 mA cm^{-2} increase of $J_{G,total}$ is visible from $\theta_p = 0°$ (corresponding to the thick perovskite configuration) to $\theta_p = 45°$. For encapsulated cells, a steep increase (~1mA cm^{-2}) in $J_{G,total}$ is observed from $\theta_p \approx 21°$. For this angle, light reflected back at the textured perovskite interface experiences total internal reflection at the glass/air interface. Therefore, light out-coupling is significantly reduced. This steep increase of $J_{G,total}$ from 21° is only visible at normal light incidence. Under realistic outdoor conditions, the annual EY increases linearly with increasing θ_p. However, already with $\theta_p = 24°$, the EY is 99.2% of the EY for the conformal perovskite configuration.

To conclude, the thick perovskite configuration provides an attractive morphology alternative, allowing a new route for the fabrication of 2T perovskite/silicon tandem solar cells. This morphology configuration combines the excellent optical properties of fully textured c-Si to the possibility to deposit the perovskite layer with cheap, flexible and up-scalable solution-based deposition techniques.

Disclosures. The authors declare no conflicts of interest.

Data availability. The complete code of the EYcalc modelling platform used for this work and the related datasets have been uploaded to GitHub [55].

Supplemental document. See Supplement 1 for supporting content.

References

1. A. Al-Ashouri, E. Köhnen, B. Li, A. Magomedov, H. Hempel, P. Caprioglio, J. A. Márquez, A. B. M. Vilches, E. Kasparavicius, J. A. Smith, N. Phung, D. Menzel, M. Grischek, L. Kegelmann, D. Skroblin, C. Gollwitzer, T. Malinauskas, M. Jošt, G. Matič, B. Rech, R. Schlatmann, M. Topič, L. Korte, A. Abate, B. Stannowski, D. Neher,

M. Stolterfoht, T. Unold, V. Getautis, and S. Albrecht, "Monolithic perovskite/silicon tandem solar cell with >29% efficiency by enhanced hole extraction," Science **370**(6522), 1300–1309 (2020).

2. "Best Research-Cell Efficiency Chart | Photovoltaic Research | NREL," https://www.nrel.gov/pv/cell-efficiency.html, accessed February 2022.

3. K. Yamamoto, K. Yoshikawa, H. Uzu, and D. Adachi, "High-efficiency heterojunction crystalline Si solar cells," in *Japanese Journal of Applied Physics* (Japan Society of Applied Physics, 2018), 57(8), p. 08RB20.

4. E. Köhnen, M. Jošt, A. B. Morales-Vilches, P. Tockhorn, A. Al-Ashouri, B. Macco, L. Kegelmann, L. Korte, B. Rech, R. Schlatmann, B. Stannowski, and S. Albrecht, "Highly efficient monolithic perovskite silicon tandem solar cells: Analyzing the influence of current mismatch on device performance," Sustain," Energy Fuels **3**(8), 1995–2005 (2019).

5. E. Aydin, T. G. Allen, M. De Bastiani, L. Xu, J. Ávila, M. Salvador, E. Van Kerschaver, and S. De Wolf, "Interplay between temperature and bandgap energies on the outdoor performance of perovskite/silicon tandem solar cells," Nat. Energy **5**(11), 851–859 (2020).

6. K. A. Bush, S. Manzoor, K. Frohna, Z. J. Yu, J. A. Raiford, A. F. Palmstrom, H. P. Wang, R. Prasanna, S. F. Bent, Z. C. Holman, and M. D. McGehee, "Minimizing Current and Voltage Losses to Reach 25% Efficient Monolithic Two-Terminal Perovskite-Silicon Tandem Solar Cells," ACS Energy Lett. **3**(9), 2173–2180 (2018).

7. Z. Wang, X. Zhu, S. Zuo, M. Chen, C. Zhang, C. Wang, X. Ren, Z. Yang, Z. Liu, X. Xu, Q. Chang, S. Yang, F. Meng, Z. Liu, N. Yuan, J. Ding, S. Liu, and D. Yang, "27%-Efficiency Four-Terminal Perovskite/Silicon Tandem Solar Cells by Sandwiched Gold Nanomesh," Adv. Funct. Mater. **30**(4), 1908298 (2020).

8. G. Coletti, S. L. Luxembourg, L. J. Geerligs, V. Rosca, A. R. Burgers, Y. Wu, L. Okel, M. Kloos, F. J. K. Danzl, M. Najafi, D. Zhang, I. Dogan, V. Zardetto, F. Di Giacomo, J. Kroon, T. Aernouts, J. Hüpkes, C. H. Burgess, M. Creatore, R. Andriessen, and S. Veenstra, "Bifacial Four-Terminal Perovskite/Silicon Tandem Solar Cells and Modules," ACS Energy Lett. **5**(5), 1676–1680 (2020).

9. S. Gharibzadeh, I. M. Hossain, P. Fassl, B. A. Nejand, T. Abzieher, M. Schultes, E. Ahlswede, P. Jackson, M. Powalla, S. Schäfer, M. Rienäcker, T. Wietler, R. Peibst, U. Lemmer, B. S. Richards, and U. W. Paetzold, "2D/3D Heterostructure for Semitransparent Perovskite Solar Cells with Engineered Bandgap Enables Efficiencies Exceeding 25% in Four-Terminal Tandems with Silicon and CIGS," Adv. Funct. Mater. **30**(19), 1909919 (2020).

10. H. A. Dewi, H. Wang, J. Li, M. Thway, R. Sridharan, R. Stangl, F. Lin, A. G. Aberle, N. Mathews, A. Bruno, and S. Mhaisalkar, "Highly Efficient Semitransparent Perovskite Solar Cells for Four Terminal Perovskite-Silicon Tandems," ACS Appl. Mater. Interfaces **11**(37), 34178–34187 (2019).

11. P. Tockhorn, P. Wagner, L. Kegelmann, J.-C. Stang, M. Mews, S. Albrecht, and L. Korte, "Three-Terminal Perovskite/Silicon Tandem Solar Cells with Top and Interdigitated Rear Contacts," ACS Appl. Energy Mater. **3**(2), 1381–1392 (2020).

12. R. Santbergen, H. Uzu, K. Yamamoto, and M. Zeman, "Optimization of Three-Terminal Perovskite/Silicon Tandem Solar Cells," IEEE J. Photovoltaics **9**(2), 446–451 (2019).

13. E. L. Warren, W. E. McMahon, M. Rienäcker, K. T. VanSant, R. C. Whitehead, R. Peibst, and A. C. Tamboli, "A Taxonomy for Three-Terminal Tandem Solar Cells," ACS Energy Lett. **5**(4), 1233–1242 (2020).

14. F. Gota, M. Langenhorst, R. Schmager, J. Lehr, and U. W. Paetzold, "Energy Yield Advantages of Three-Terminal Perovskite-Silicon Tandem Photovoltaics," Joule **4**(11), 2387–2403 (2020).

15. F. Sahli, B. A. Kamino, J. Werner, M. Bräuninger, B. Paviet-Salomon, L. Barraud, R. Monnard, J. P. Seif, A. Tomasi, Q. Jeangros, A. Hessler-Wyser, S. De Wolf, M. Despeisse, S. Nicolay, B. Niesen, and C. Ballif, "Improved Optics in Monolithic Perovskite/Silicon Tandem Solar Cells with a Nanocrystalline Silicon Recombination Junction," Adv. Energy Mater. **8**(6), 1701609 (2018).

16. J. P. Mailoa, C. D. Bailie, E. C. Johlin, E. T. Hoke, A. J. Akey, W. H. Nguyen, M. D. McGehee, and T. Buonassisi, "A 2-terminal perovskite/silicon multijunction solar cell enabled by a silicon tunnel junction," Appl. Phys. Lett. **106**(12), 121105 (2015).

17. B. Chen, N. Ren, Y. Li, L. Yan, S. Mazumdar, Y. Zhao, and X. Zhang, "Insights into the Development of Monolithic Perovskite/Silicon Tandem Solar Cells," Adv. Energy Mater. **12**(4), 2003628 (2022).

18. J. Werner, B. Niesen, and C. Ballif, "Perovskite/Silicon Tandem Solar Cells: Marriage of Convenience or True Love Story? – An Overview," Adv. Mater. Interfaces **5**(1), 1700731 (2018).

19. J. Lehr, M. Langenhorst, R. Schmager, S. Kirner, U. Lemmer, B. S. Richards, C. Case, and U. W. Paetzold, "Energy yield modelling of perovskite/silicon two-terminal tandem PV modules with flat and textured interfaces," Sustain Energy Fuels **2**(12), 2754–2761 (2018).

20. D. A. Jacobs, M. Langenhorst, F. Sahli, B. S. Richards, T. P. White, C. Ballif, K. R. Catchpole, and U. W. Paetzold, "Light Management: A Key Concept in High-Efficiency Perovskite/Silicon Tandem Photovoltaics," J. Phys. Chem. Lett. **10**(11), 3159–3170 (2019).

21. W. McMahon, H. Schulte-Huxel, J. Buencuerpo, J. Geisz, M. Young, T. Klein, A. Tamboli, and E. Warren, "Homogenous Voltage-Matched Strings Using Three-Terminal Tandem Solar Cells: Fundamentals and End Losses," IEEE J. Photovoltaics **11**(4), 1078–1086 (2021).

22. "ITRPV - VDMA," https://itrpv.vdma.org/en/, accessed November 2021.

23. T. Duong, Y. Wu, H. Shen, J. Peng, X. Fu, D. Jacobs, E.-C. Wang, T. C. Kho, K. C. Fong, M. Stocks, E. Franklin, A. Blakers, N. Zin, K. McIntosh, W. Li, Y.-B. Cheng, T. P. White, K. Weber, and K. Catchpole, "Rubidium Multication

Perovskite with Optimized Bandgap for Perovskite-Silicon Tandem with over 26% Efficiency," Adv. Energy Mater. **7**(14), 1700228 (2017).

24. L. Gil-Escrig, M. Roß, J. Sutter, A. Al-Ashouri, C. Becker, and S. Albrecht, "Fully Vacuum-Processed Perovskite Solar Cells on Pyramidal Microtextures," Sol. RRL **5**(1), 2000553 (2021).

25. T. Abzieher, J. A. Schwenzer, S. Moghadamzadeh, F. Sutterluti, J. A. Schwenzer, I. M. Hossain, M. Pfau, E. Lotter, M. Hetterich, B. S. Richards, U. Lemmer, M. Powalla, and U. W. Paetzold, "Efficient All-Evaporated pin-Perovskite Solar Cells: A Promising Approach Toward Industrial Large-Scale Fabrication," IEEE J. Photovoltaics **9**(5), 1249–1257 (2019).

26. B. Chen, Z. J. Yu, S. Manzoor, S. Wang, W. Weigand, Z. Yu, G. Yang, Z. Ni, X. Dai, Z. C. Holman, and J. Huang, "Blade-Coated Perovskites on Textured Silicon for 26%-Efficient Monolithic Perovskite/Silicon Tandem Solar Cells," Joule **4**(4), 850–864 (2020).

27. A. S. Subbiah, F. H. Isikgor, C. T. Howells, M. De Bastiani, J. Liu, E. Aydin, F. Furlan, T. G. Allen, F. Xu, S. Zhumagali, S. Hoogland, E. H. Sargent, I. McCulloch, and S. De Wolf, "High-performance perovskite single-junction and textured perovskite/silicon tandem solar cells via slot-die-coating," ACS Energy Lett. **5**(9), 3034–3040 (2020).

28. S. Sansoni, M. De Bastiani, E. Aydin, E. Ugur, F. H. Isikgor, A. Al-Zahrani, F. Lamberti, F. Laquai, M. Meneghetti, and S. De Wolf, "Eco-Friendly Spray Deposition of Perovskite Films on Macroscale Textured Surfaces," Adv. Mater. Technol. **5**(2), 1901009 (2020).

29. M. K. Basher, M. K. Hossain, M. J. Uddin, M. A. R. Akand, and K. M. Shorowordi, "Effect of pyramidal texturization on the optical surface reflectance of monocrystalline photovoltaic silicon wafers," Optik **172**, 801–811 (2018).

30. M. Jošt, L. Kegelmann, L. Korte, and S. Albrecht, "Monolithic Perovskite Tandem Solar Cells: A Review of the Present Status and Advanced Characterization Methods Toward 30% Efficiency," Adv. Energy Mater. **10**(26), 1904102 (2020).

31. L. Mazzarella, Y. Lin, S. Kirner, A. B. Morales-Vilches, L. Korte, S. Albrecht, E. Crossland, B. Stannowski, C. Case, H. J. Snaith, and R. Schlatmann, "Infrared Light Management Using a Nanocrystalline Silicon Oxide Interlayer in Monolithic Perovskite/Silicon Heterojunction Tandem Solar Cells with Efficiency above 25%," Adv. Energy Mater. **9**(14), 1803241 (2019).

32. Z. J. Yu, B. M. Wheelwright, S. Manzoor, and Z. C. Holman, "Silicon wafers with optically specular surfaces formed by chemical polishing," J Mater Sci: Mater Electron **27**(10), 10270–10275 (2016).

33. F. Sahli, J. Werner, B. A. Kamino, M. Bräuninger, R. Monnard, B. Paviet-Salomon, L. Barraud, L. Ding, J. J. Diaz Leon, D. Sacchetto, G. Cattaneo, M. Despeisse, M. Boccard, S. Nicolay, Q. Jeangros, B. Niesen, and C. Ballif, "Fully textured monolithic perovskite/silicon tandem solar cells with 25.2% power conversion efficiency," Nat. Mater. **17**(9), 820–826 (2018).

34. Y. Hou, E. Aydin, M. De Bastiani, C. Xiao, F. H. Isikgor, D.-J. Xue, B. Chen, H. Chen, B. Bahrami, A. H. Chowdhury, A. Johnston, S.-W. Baek, Z. Huang, M. Wei, Y. Dong, J. Troughton, R. Jalmood, A. J. Mirabelli, T. G. Allen, E. Van Kerschaver, M. I. Saidaminov, D. Baran, Q. Qiao, K. Zhu, S. De Wolf, and E. H. Sargent, "Efficient tandem solar cells with solution-processed perovskite on textured crystalline silicon," Science **367**(6482), 1135–1140 (2020).

35. M. De Bastiani, A. J. Mirabelli, Y. Hou, F. Gota, E. Aydin, T. G. Allen, J. Troughton, A. S. Subbiah, F. H. Isikgor, J. Liu, L. Xu, B. Chen, E. Van Kerschaver, D. Baran, B. Fraboni, M. F. Salvador, U. W. Paetzold, E. H. Sargent, and S. De Wolf, "Efficient bifacial monolithic perovskite/silicon tandem solar cells via bandgap engineering," Nat. Energy **6**(2), 167–175 (2021).

36. E. Aydin, J. Liu, E. Ugur, R. Azmi, G. T. Harrison, Y. Hou, B. Chen, S. Zhumagali, M. De Bastiani, M. Wang, W. Raja, T. G. Allen, A. ur Rehman, A. S. Subbiah, M. Babics, A. Babayigit, F. H. Isikgor, K. Wang, E. Van Kerschaver, L. Tsetseris, E. H. Sargent, F. Laquai, and S. De Wolf, "Ligand-bridged charge extraction and enhanced quantum efficiency enable efficient n–i–p perovskite/silicon tandem solar cells," Energy Environ. Sci. **14**, 4377–4390 (2021).

37. J. Liu, E. Aydin, J. Yin, M. De Bastiani, F. H. Isikgor, A. U. Rehman, E. Yengel, E. Ugur, G. T. Harrison, M. Wang, Y. Gao, J. I. Khan, M. Babics, T. G. Allen, A. S. Subbiah, K. Zhu, X. Zheng, W. Yan, F. Xu, M. F. Salvador, O. M. Bakr, T. D. Anthopoulos, M. Lanza, O. F. Mohammed, F. Laquai, and S. De Wolf, "28.2%-efficient, outdoor-stable perovskite/silicon tandem solar cell," Joule **5**(12), 3169–3186 (2021).

38. H. Eggers, F. Schackmar, T. Abzieher, Q. Sun, U. Lemmer, Y. Vaynzof, B. S. Richards, G. Hernandez-Sosa, and U. W. Paetzold, "Inkjet-Printed Micrometer-Thick Perovskite Solar Cells with Large Columnar Grains," Adv. Energy Mater. **10**(6), 1903184 (2020).

39. B. Chen, S. W. Baek, Y. Hou, E. Aydin, M. De Bastiani, B. Scheffel, A. Proppe, Z. Huang, M. Wei, Y. K. Wang, E. H. Jung, T. G. Allen, E. Van Kerschaver, F. P. García de Arquer, M. I. Saidaminov, S. Hoogland, S. De Wolf, and E. H. Sargent, "Enhanced optical path and electron diffusion length enable high-efficiency perovskite tandems," Nat. Commun. **11**(1), 1–9 (2020).

40. Y. Vaynzof, "The Future of Perovskite Photovoltaics—Thermal Evaporation or Solution Processing?" Adv. Energy Mater. **10**(48), 2003073 (2020).

41. R. Schmager, U. W. Paetzold, M. Langenhorst, F. Gota, and J. Lehr, "EYcalc - Energy yield calculator for multi-junction solar modules with realistic irradiance data and textured interfaces," Zenodo (2021), https://doi.org/10.5281/zenodo.4696257.

42. R. Schmager, M. Langenhorst, J. Lehr, U. Lemmer, B. S. Richards, and U. W. Paetzold, "Methodology of energy yield modelling of perovskite-based multi-junction photovoltaics," Opt. Express **27**(8), A507 (2019).

43. L. Krückemeier, U. Rau, M. Stolterfoht, and T. Kirchartz, "How to Report Record Open-Circuit Voltages in Lead-Halide Perovskite Solar Cells," Adv. Energy Mater. **10**(1), 1902573 (2020).

44. G. Nogay, F. Sahli, J. Werner, R. Monnard, M. Boccard, M. Despeisse, F. J. Haug, Q. Jeangros, A. Ingenito, and C. Ballif, "25.1%-Efficient monolithic perovskite/silicon tandem solar cell based on a p-type monocrystalline textured silicon wafer and high-temperature passivating contacts," ACS Energy Lett. **4**(4), 844–845 (2019).

45. S. Wilcox and W. Marion, "Innovation for Our Energy Future," in *Users Manual for TMY3 Data Sets* (National Renewable Energy Laboratory, 1994).

46. C. A. Gueymard, "Parameterized transmittance model for direct beam and circumsolar spectral irradiance," Sol. Energy **71**(5), 325–346 (2001).

47. S. C. Baker-Finch and K. R. McIntosh, "Reflection of normally incident light from silicon solar cells with pyramidal texture," Prog. Photovolt: Res. Appl. **19**(4), 406–416 (2011).

48. "LTspice | Design Center | Analog Devices," https://www.analog.com/en/design-center/design-tools-and-calculators/ltspice-simulator.html#., accessed November 2021.

49. M. C. Alonso García and J. L. Balenzategui, "Estimation of photovoltaic module yearly temperature and performance based on Nominal Operation Cell Temperature calculations," Renew. Energy **29**(12), 1997–2010 (2004).

50. M. Jošt, E. Köhnen, A. B. Morales-Vilches, B. Lipovšek, K. Jäger, B. Macco, A. Al-Ashouri, J. Krč, L. Korte, B. Rech, R. Schlatmann, M. Topič, B. Stannowski, and S. Albrecht, "Textured interfaces in monolithic perovskite/silicon tandem solar cells: Advanced light management for improved efficiency and energy yield," Energy Environ. Sci. **11**(12), 3511–3523 (2018).

51. S. Albrecht, M. Saliba, J. P. Correa-Baena, K. Jäger, L. Korte, A. Hagfeldt, M. Grätzel, and B. Rech, "Towards optical optimization of planar monolithic perovskite/silicon-heterojunction tandem solar cells," J. Opt. **18**(6), 064012 (2016).

52. A. Alasfour, Z. J. Yu, W. Weigand, D. Quispe, and Z. C. Holman, "Sub-micrometer random-pyramid texturing of silicon solar wafers with excellent surface passivation and low reflectance," Sol. Energy Mater. Sol. Cells **218**, 110761 (2020).

53. T. C.-J. Yang, P. Fiala, Q. Jeangros, and C. Ballif, "High-Bandgap Perovskite Materials for Multijunction Solar Cells," Joule **2**(8), 1421–1436 (2018).

54. M. Langenhorst, B. Sautter, R. Schmager, J. Lehr, E. Ahlswede, M. Powalla, U. Lemmer, B. S. Richards, and U. W. Paetzold, "Energy yield of all thin-film perovskite/CIGS tandem solar modules," Prog. Photovolt. **27**, 290–298 (2018).

55. R. Schmager, M. Lagenhorst, J. Lehr, and F. Gota, "EYcalc," Github (2022), https://github.com/PerovskitePV/EYcalc.